

ULTRASOUND NEWS

February 2022



Transthoracic ultrasound shear wave elastography for the study of subpleural lung lesions

Carla Maria Irene Quarato¹, Mariapia Venuti¹, Lucia Dimitri², Donato Lacedonia¹, Anna Simeone³, Antonio Mirijello⁴, Salvatore De Cosmo⁴, Evaristo Maiello⁵, Marco Turchini⁶, Giulia Scioscia¹, Maria Pia Foschino Barbaro¹, Massimiliano Copetti⁷, Marco Sperandio⁸

¹Department of Medical and Surgical Sciences, Institute of Respiratory Diseases, Policlinico Riuniti di Foggia, University of Foggia, Foggia; ²Unit of Pathology, ³Department of Radiology, ⁴Department of Internal Medicine, ⁵Unit of Oncology, ⁶Unit of Thoracic Surgery, ⁷Unit of Biostatistics, ⁸Unit of Interventional and Diagnostic Ultrasound, Department of Internal Medicine, IRCCS Fondazione Casa Sollievo della Sofferenza, San Giovanni Rotondo, Foggia, Italy

ULTRA SONO GRAPHY

ORIGINAL ARTICLE

<https://doi.org/10.14366/usg.21021>

pISSN: 2288-5919 • eISSN: 2288-5943

Ultrasonography 2022;41:93-105

Received: January 29, 2021

Revised: March 22, 2021

Accepted: April 15, 2021

Correspondence to:

.....

Purpose: The aim of this study was to assess whether new-generation shear wave elastography (SWE) is suitable for the characterization of lung subpleural lesions.

Methods: In total, 190 consecutive patients with subpleural lung lesions received ultrasonography and SWE. Patients with suspected malignancy underwent ultrasound-guided transthoracic needle biopsy. Final diagnoses were made on the basis of patients' clinical course, microbiological studies, and histological results. SWE was also performed in 25 healthy volunteers.

Results: We found no statistically significant differences in stiffness between lung carcinomas, lung metastases, and pneumonia ($P=0.296$) or between different histological types of lung cancer ($P=0.393$). Necrosis was associated with reduced stiffness in pneumonia. Excluding necrotic lesions, pneumonia showed higher stiffness than lung carcinomas (2.95 ± 0.68 m/s vs. 2.60 ± 0.54 m/s, $P=0.006$). Chronic pneumonia showed increased stiffness (3.03 ± 0.63 m/s), probably due to the presence of fibrotic tissue on histology. Pleural effusion was associated with a statistically significant reduction in stiffness, both in lung carcinomas ($P=0.004$) and lung metastases ($P=0.002$). The presence of air in healthy lung tissue may lead to incorrect speed estimates due to shear wave reflection (very high values, 14.64 ± 2.19 m/s).

Conclusion: Transthoracic SWE could not distinguish lung malignancy from pneumonia, or between different histological types of lung carcinomas. In particular, SWE seems unable to resolve the clinical dilemma of chronic subpleural consolidations.



Fig. 2. An example of a thoracic ultrasonography (TUS) and shear wave elastography examination followed by ultrasonography-guided transthoracic needle biopsy.

A. Computed tomography scan of a left lung subpleural lesion that proved to be malignant (arrowhead) is shown. **B.** Ultrasonography with a convex probe (6 MHz) of the same nodular lesion (2.1 cm) shows an irregular hypoechoic pattern. **C.** Color-coded two dimensional elastography map of the lesion (arrow) is created. **D.** Elastographic measurements were performed. On the monitor, in the left, are displayed 10 consecutive shear wave measurement in m/s, their median value and the interquartile range/median ratio (IQR/M). During each measurement a small fixed region of interest (ROI) of 1×1 cm (arrow) was selected. The relative three dimensional elastography map is color-coded based on the amount of tissue displacement in the selected ROI: tissue stiffness is indicated by a blue color occupying >85% of the area. **E.** Convex probe with a central hole for needle insertion is shown. **F.** TUS-guided needle biopsy was performed. It is possible to see the needle tip in the nodule (arrow). **G.** Biopsy specimen to obtain sufficient material for both cytology and histology analyses is shown.

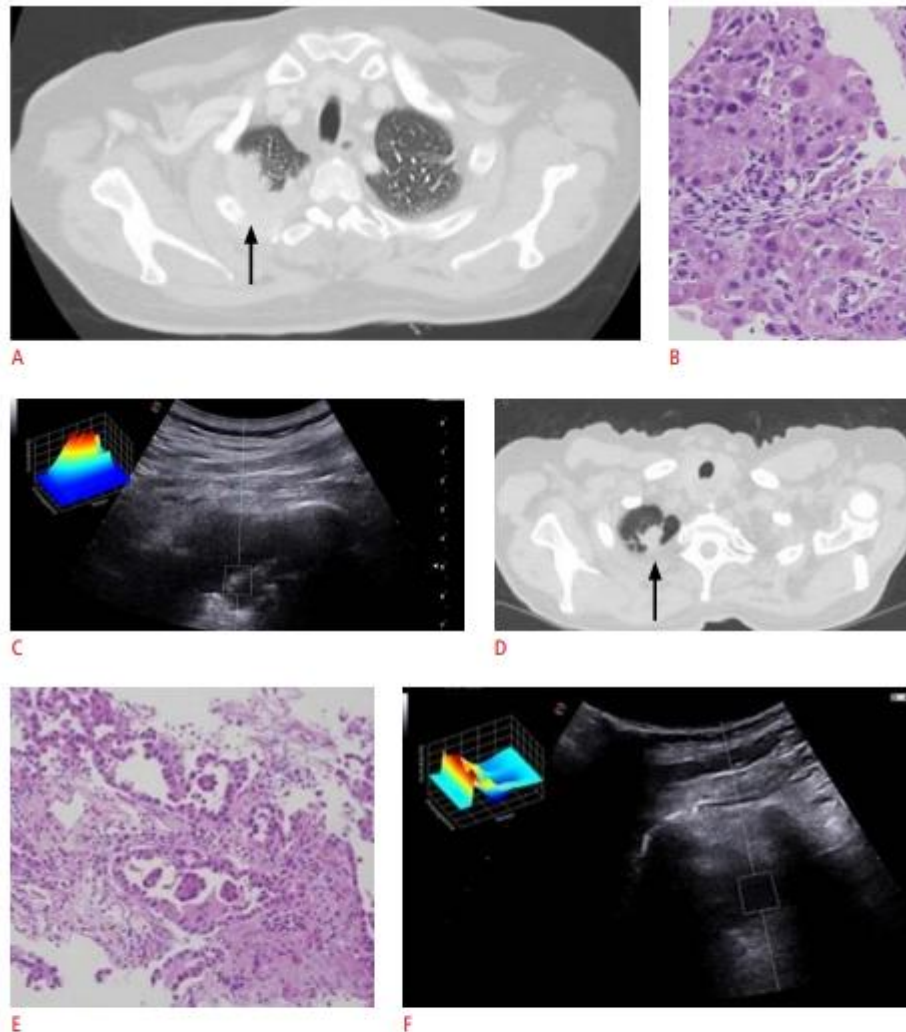
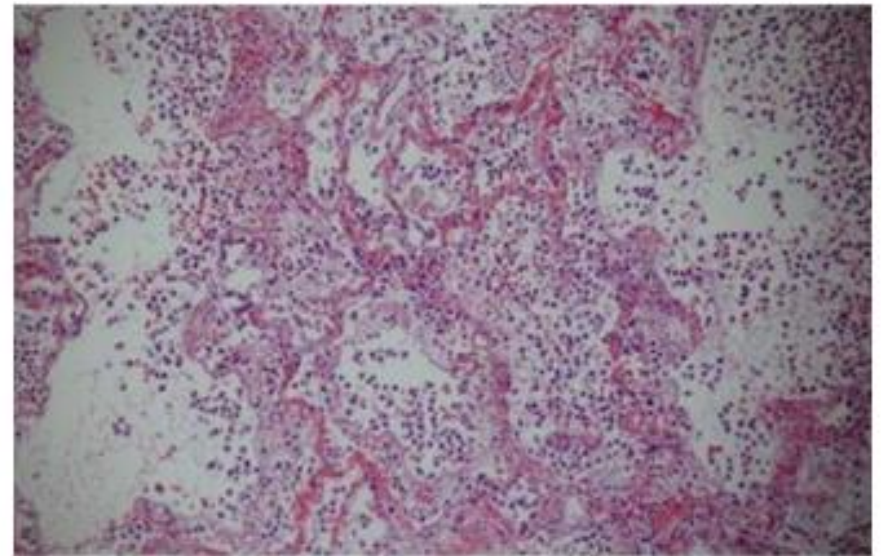


Fig. 3. Shear wave elastography (SWE) examination of malignant lesions.

A. Computed tomography (CT) scan shows a lung lesion suspected of malignancy in the posterior upper right lobe (arrow). **B.** Histology reveals a diagnosis of lung squamous cell carcinoma (H&E, $\times 600$). **C.** B-mode ultrasound (US) using a convex probe (6 MHz) shows an irregular subpleural consolidation with an inhomogeneous pattern. The three-dimensional elastography map in the left side is color-coded based on the amount of tissue displacement: the center of the region of interest shows high strain, encoded as red (soft tissue), while its peripheral part is blue (low strain, stiff tissue). The mean SWE value in the entire lesion was 2.8 m/s. **D.** CT scan shows a lung subpleural lesion in the apical upper right lobe (arrow). **E.** Histology reveals a diagnosis of lung adenocarcinoma (H&E, $\times 600$). **F.** US imaging with a convex probe (6 MHz) shows an irregular mixed hypoechoic and hyperechoic pattern. The relative three-dimensional color-coded US elastography map of the region of interest shows an asymmetrical area of soft tissue (red) on a light blue background (intermediate stiff tissue). The mean SWE value in the entire lesion was 2.6 m/s.



A



B

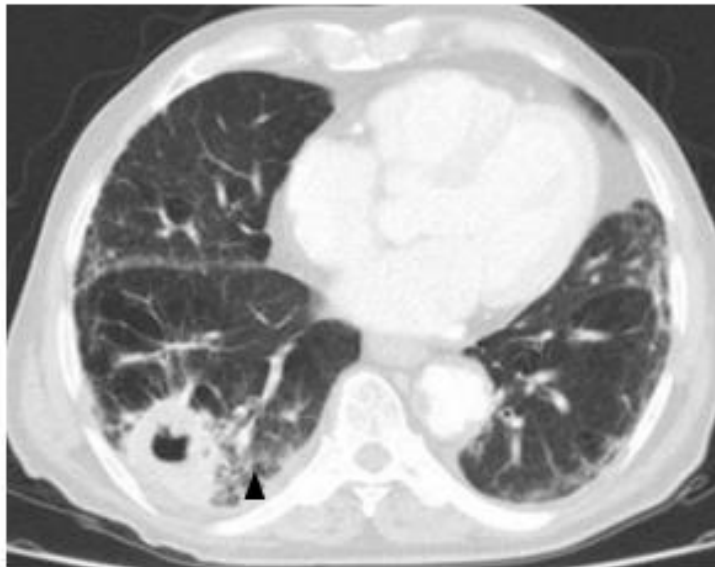


C

Fig. 4. Shear wave elastography (SWE) examination in pneumonia.

A. Computed tomography scan shows a bilateral pneumonia. The left lesion (arrow) was selected for subsequent examinations.

B. Histology reveals a diagnosis of chronic pneumonia showing a mixture of chronic inflammatory cells and fibroblasts within airspaces (H&E, $\times 200$). **C.** The B-mode ultrasound (US) using a convex probe (6 MHz) shows hypoechoic/anechoic consolidation with hyperechoic spots/striae within. The relative three-dimensional US elastography color-coded map of the region of interest shows a central area of low strain (hard tissue), encoded as blue, surrounded by a peripheral area of intermediate stiffness (yellow). The mean SWE value of the entire lesion was 3.3 m/s.



A




B

Fig. 5. Shear wave elastography (SWE) examinations in a necrotic lesion.





A. Computed tomography scan shows a lung lesion with central necrosis in the lower right lobe (arrowhead). **B.** The B-mode ultrasound (US) using a convex probe (6 MHz) shows a hypoechoic consolidation with hyperechoic spots/striae within and a central anechoic area (arrow). The relative three-dimensional US elastography color-coded map of the region of interest shows a central area of high strain encoded as red (soft tissue) on a background of intermediate stiffness encoded as green/light blue. The mean SWE value in the entire lesion was 2.7 m/s.

[Home](#) > [Radiology](#) > [Recently Published](#)[< PREVIOUS](#)[NEXT >](#)

Original Research
Pediatric Imaging

 **Free Access**

Statistical Shape Modeling of US Images to Predict Hip Dysplasia Development in Infants

 Joshua M. Bonsel,  Willem Paul Gielis, Virginie Pollet, Harrie H. Weinans,  Ralph J.B. Sakkars 

▼ [Author Affiliations](#)

Published Online: Jan 25 2022 | <https://doi.org/10.1148/radiol.211057>

Statistical Shape Modeling of US Images to Predict Hip Dysplasia Development in Infants

Joshua M. Bonse, MD • Willem Paul Gielis, MD • Virginie Pollet, MD, PhD • Harrie H. Weinans, MD, PhD • Ralph J.B. Sakkers, MD, PhD

From the Department of Orthopedic Surgery, University Medical Center Utrecht, Lundlaan 6, 3584EA, Utrecht, the Netherlands (J.M.B., W.P.G., H.H.W., R.J.B.S.); Department of Orthopedic Surgery, Erasmus Medical Center, Rotterdam, the Netherlands (J.M.B.); and Department of Pediatric Orthopedic Surgery, Royal Manchester Children's Hospital, Manchester, United Kingdom (V.P.). Received April 30, 2021; revision requested July 6; revision received October 28; accepted November 16. Address correspondence to R.J.B.S. (e-mail: r.sakkers@umcutrecht.nl).

Conflicts of interest are listed at the end of this article.

Radiology 2022; 000:1–8 • <https://doi.org/10.1148/radiol.211057> • Content codes: MK PD

Background: The current widely applied Graf classification used on US images for developmental dysplasia of the hip in infants does not enable prediction of the development and outcome of well-centered stable dysplastic hips (Graf type II).

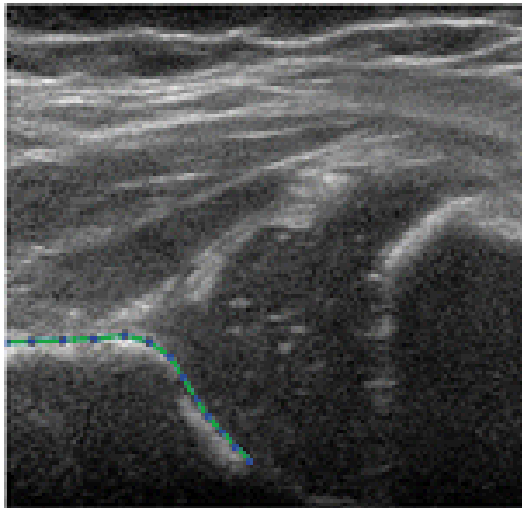
Purpose: To use statistical shape modeling on US images to identify acetabular shape characteristics of Graf type II hips, which enable prediction of the development of Graf type II hips, and to identify which hips benefit from Pavlik harness treatment.

Materials and Methods: In this secondary analysis of a prospective multicenter randomized trial on treatment of 104 infants aged 3–4 months with Graf type IIb or IIc hip dysplasia conducted between 2009 and 2015, a statistical shape model was developed on baseline US images. With multivariable logistic regression adjusted for infant sex and treatment (Pavlik harness treatment vs active observation), shape modes were correlated with the outcomes of persistent hip dysplasia on US images (α angle $< 60^\circ$) after 12-week follow-up and residual hip dysplasia on pelvic radiographs (Tönnis classification: acetabular index greater than 2 standard deviations) around 1 year of age. An interaction term (treatment with mode) was used to investigate if this result depended on treatment.

Results: Baseline US images were available in 97 infants (mean age, 3.37 years \pm 0.43 [standard deviation]; 89 [92%] girls; 90 cases of Graf type IIb hip dysplasia; 52 cases treated with Pavlik harness). Shape modes 2 and 3 of the statistical shape modeling were associated with persistent hip dysplasia on US images (odds ratio [OR] = 0.43; P = .007 and OR = 2.39; P = .02, respectively). Mode 2 was also associated with residual hip dysplasia on pelvic radiographs (OR = 0.09; P = .002). The interaction term remained significant after multivariable analysis, indicating that Pavlik harness treatment was beneficial in patients with negative mode 2 values (OR = 12.46; P = .01).

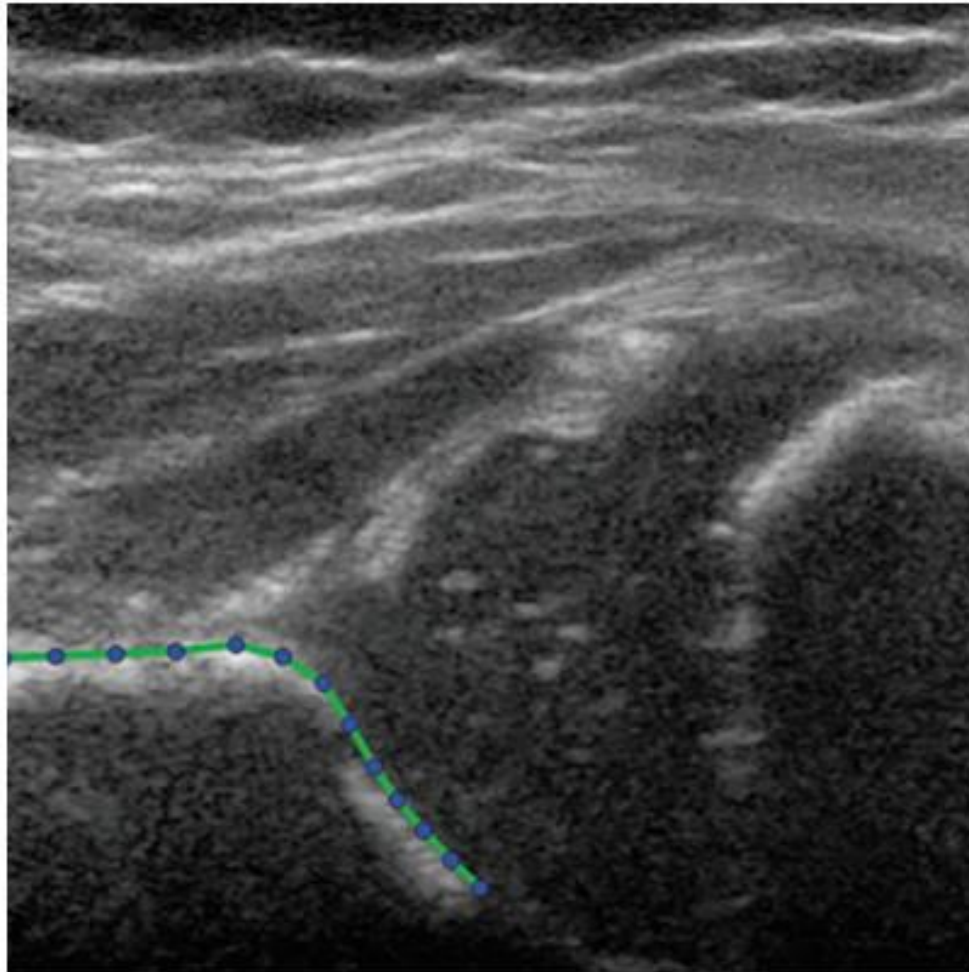
Conclusion: Statistical shape modeling of US images of infants with Graf type II dysplastic hips predicted which hips developed to normal or remained dysplastic and identified hips that benefited from Pavlik harness treatment.

Statistical Shape Modelling of US Images to Predict Hip Dysplasia Development in Infants



Hip US image in a 3-month-old girl at baseline. No contrast material was used. The hip is outlined with the acetabular shape model, consisting of 13 points.

- In this secondary analysis of a randomized trial, statistical shape modelling of US images of 97 well-centered stable dysplastic hips predicted which hips developed to normal or remained dysplastic.
- After 12 weeks, modes 2 (odds ratio [OR] = 0.43, $P = .007$) and 3 (OR = 2.39, $P = .02$) were associated with dysplasia on US images irrespective of Pavlik harness treatment.
- Around 1 year of age, mode 2 was associated with dysplasia on radiographs (OR = 0.09, $P = .002$), but this was counteracted by Pavlik harness treatment (OR = 12.46, $P = .01$).



Hip ultrasound image in a 3-month-old girl at baseline. No contrast material was used. The presented hip is outlined with the acetabular shape model, consisting of 13 points. The researchers wrote that through statistical shape modeling from ultrasound images, hip dysplasia, and treatment can be better predicted. Image courtesy of RSNA.



Figure 4: Examples of hip US images obtained with mode 1; no contrast material was used. The presented hips were **(A)** -1.58 [girl], **(B)** +0.11 [girl], and **(C)** +1.80 [boy] standard deviations from the mean shape.

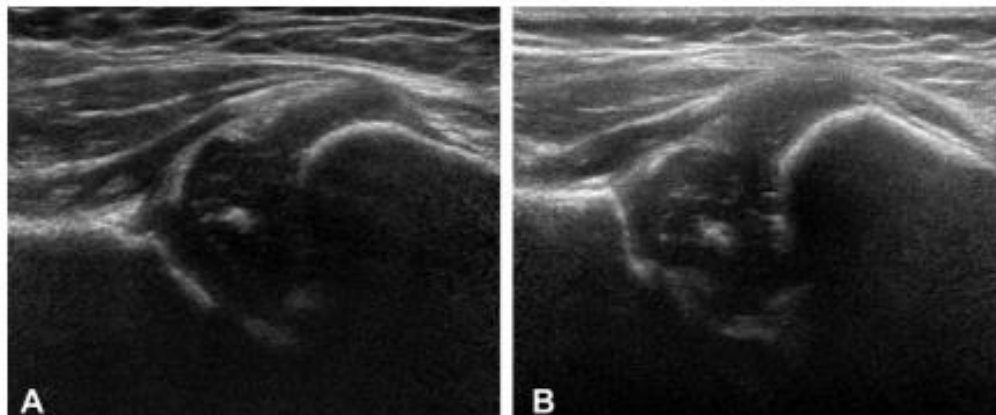


Figure 5: Examples of hip US images acquired with mode 2; no contrast material was used. The presented hips were **(A)** -1.83 [girl] and **(B)** +2.12 [girl] standard deviations from the mean shape.

[Home](#) > [American Journal of Roentgenology](#) > [Volume 216, Issue 1](#) >

[Ultrasound Of Musculoskeletal Hematomas: Relationship Of Sonographic Appearance To Age And Ease Of Aspiration](#)



January 2021, VOLUME 216
NUMBER 1

January 2021, Volume 216, Number 1

Musculoskeletal Imaging
Original Research

[« Previous Article](#) | [Next Article »](#)

Ultrasound of Musculoskeletal Hematomas: Relationship of Sonographic Appearance to Age and Ease of Aspiration

Edward S. Yoon, MD¹, Bin Lin, PhD¹ and Theodore T. Miller, MD¹

Share

Claim CREDIT

+ Affiliation:

Citation: American Journal of Roentgenology. 2021;216: 125-130. 10.2214/AJR.19.22752

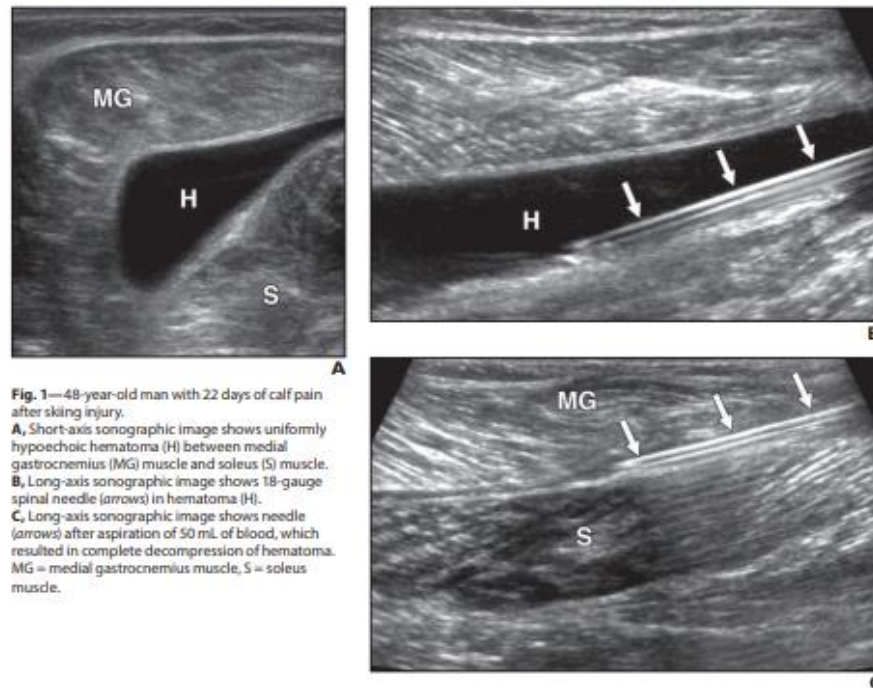


Fig. 1—48-year-old man with 22 days of calf pain after skiing injury.
A, Short-axis sonographic image shows uniformly hypoechoic hematoma (H) between medial gastrocnemius (MG) muscle and soleus (S) muscle.
B, Long-axis sonographic image shows 18-gauge spinal needle (arrows) in hematoma (H).
C, Long-axis sonographic image shows needle (arrows) after aspiration of 50 mL of blood, which resulted in complete decompression of hematoma. MG = medial gastrocnemius muscle, S = soleus muscle.

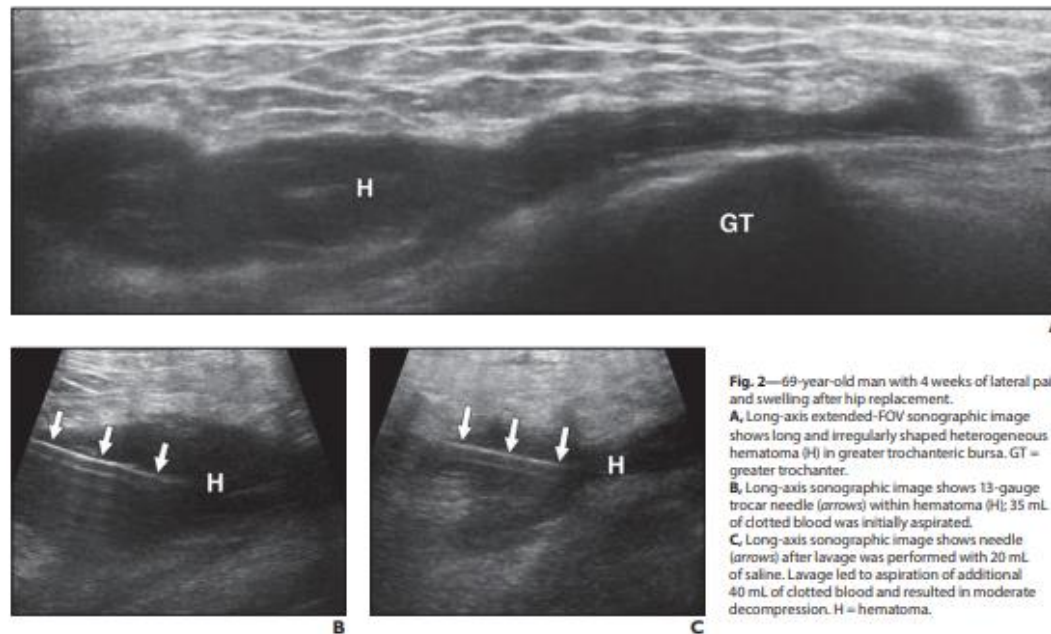


Fig. 2—69-year-old man with 4 weeks of lateral pain and swelling after hip replacement.
A, Long-axis extended-FOV sonographic image shows long and irregularly shaped heterogeneous hematoma (H) in greater trochanteric bursa. GT = greater trochanter.
B, Long-axis sonographic image shows 13-gauge trocar needle (arrows) within hematoma (H); 35 mL of clotted blood was initially aspirated.
C, Long-axis sonographic image shows needle (arrows) after lavage was performed with 20 mL of saline. Lavage led to aspiration of additional 40 mL of clotted blood and resulted in moderate decompression. H = hematoma.

ABSTRACT

- **OBJECTIVE.** The purpose of this study was to evaluate the safety and efficacy of ultrasound-guided aspiration of musculoskeletal hematomas, evaluate the associations between the sonographic appearance of hematomas and their age with ease of aspiration, and determine if there is an optimal time frame for aspiration.
- **MATERIALS AND METHODS.** A retrospective search of our radiology database was conducted using the keywords “hematoma” and “aspiration” for procedures performed from January 1, 2008, through September 28, 2017, by three fellowship-trained musculoskeletal radiologists. Associations between the ease of aspiration and echotexture of the hematoma and between the ease of aspiration and age of the hematoma were assessed with a marginal ordinal logistic regression model to account for patient-level clusters. Pairwise comparisons of the ease of aspiration between the different echotextures were adjusted for multiple comparisons with the Tukey-Kramer method. This same method was also used to calculate the odds ratio (OR) for the age of the hematoma and ease of aspiration and decompression. Clinical follow-up was assessed for infection and symptomatic relief.
- **RESULTS.** The cohort was composed of 148 patients (77 male and 71 female patients) with a mean age of 48 years (age range, 16–80 years). One hundred patients underwent clinical follow-up: There were no instances of infection and all patients reported symptomatic relief. Marginal proportional odds model showed an OR of 3.77 when comparing the ease of aspiration between hypoechoic hematomas and hematomas showing the other echotextures combined (i.e., complex, heterogeneous, echo-genic), which was statistically significant ($p = 0.010$). The OR of the ease of aspiration in relation to the age of a hematoma for each additional week was 1.03 with a p value of 0.547, which shows that there is no correlation between the age of the hematoma and ease of aspiration.
- **CONCLUSION.** Ultrasound-guided aspiration of hematomas is a safe and effective procedure. The sonographic appearance of a hematoma is unrelated to its age. Although a hematoma with a hypoechoic appearance is easier to aspirate than hematomas with other echotextures, the appearance and age of a hematoma should not dissuade one from trying to aspirate it.
-

Read

More: https://www.ajronline.org/doi/full/10.2214/AJR.19.22752?utm_campaign=roentgen+journal&utm_medium=email&utm_source=informz

Combined accuracy of optic nerve sheath diameter, strain ratio, and shear wave elastography of the optic nerve in patients with idiopathic intracranial hypertension

Ahmed Abdel Khalek Abdel Razek¹, Nada Elsaid², Tamer Belal², Nihal Batouty¹,
Ahmed Azab²

Departments of ¹Diagnostic Radiology and ²Neurology, Mansoura Faculty of Medicine,
Mansoura, Egypt

Purpose: This study assessed the combined accuracy of optic nerve sheath diameter (ONSD), strain ratio (SR), and shear wave elastography (SWE) of the optic nerve (ON) in patients with idiopathic intracranial hypertension (IIH).

Methods: This prospective study was carried out on both ONs of 34 consecutive patients diagnosed with IIH and 16 age- and sex-matched healthy volunteers. All of the study participants were women. The ONSD, SR, and SWE of the ON were measured. The severity of papilledema of IIH patients was sub-classified into mild papilledema and moderate/severe papilledema.

Results: The mean ONSD (5.6 ± 1.1 mm), SR (0.7 ± 0.1), and SWE (30.1 ± 16.7 kPa) of the IIH patients were significantly different ($P=0.001$) from the ONSD (4.1 ± 0.5 mm), SR (0.9 ± 0.1), and SWE (8.2 ± 3.4 kPa) of controls. The cutoff values of ONSD, SR, and SWE of the ON for differentiating IIH patients from controls were 5.45 mm, 0.8, and 10.3 kPa with areas under the curve (AUCs) of 0.91, 0.86, and 0.96 and accuracy values of 91%, 81%, and 93%, respectively. Combined SWE and ONSD and combined SWE, ONSD, and SR for differentiating IIH patients from controls revealed AUCs of 0.98 and 0.99 and accuracy values of 96% and 96%, respectively. ONSD, SR, and SWE showed significant differences between mild and moderate/severe papilledema ($P=0.001$). Papilledema was correlated with SWE ($r=0.8$, $P=0.001$), ONSD ($r=0.4$, $P=0.001$), and SR ($r=-0.4$, $P=0.001$).

Conclusion: The combination of ONSD, SR, and SWE may be helpful for diagnosing IIH, and a good indicator of the degree of papilledema.

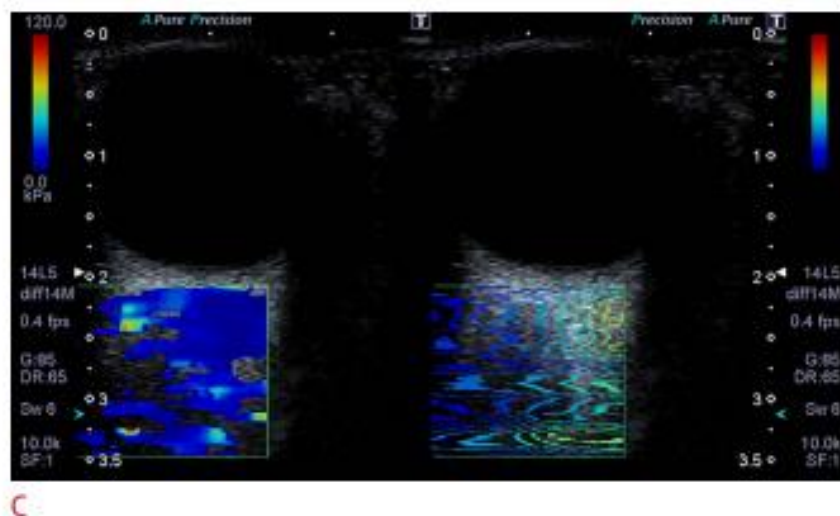
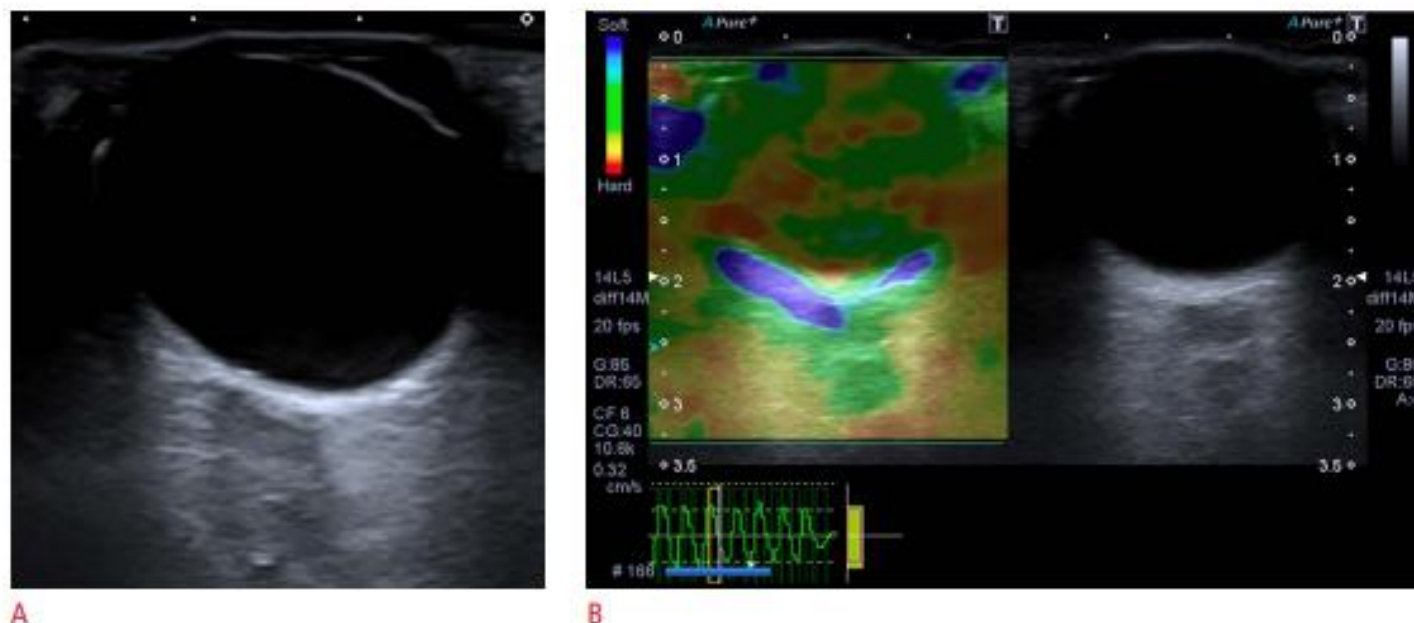
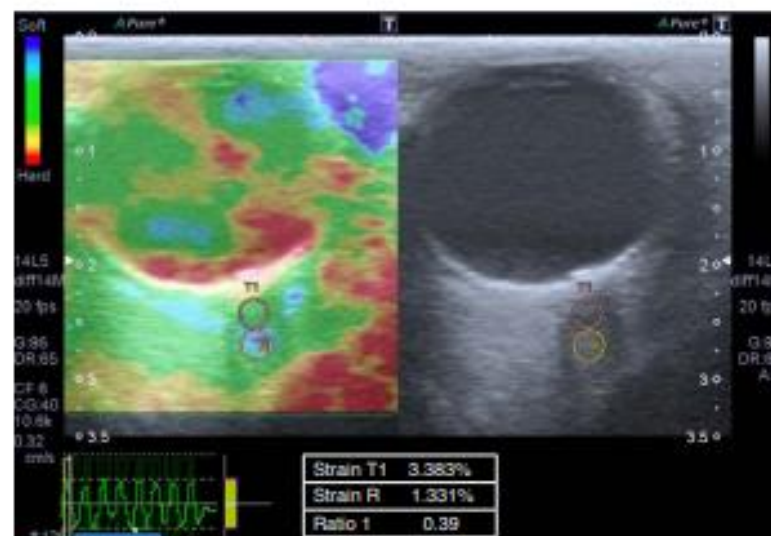


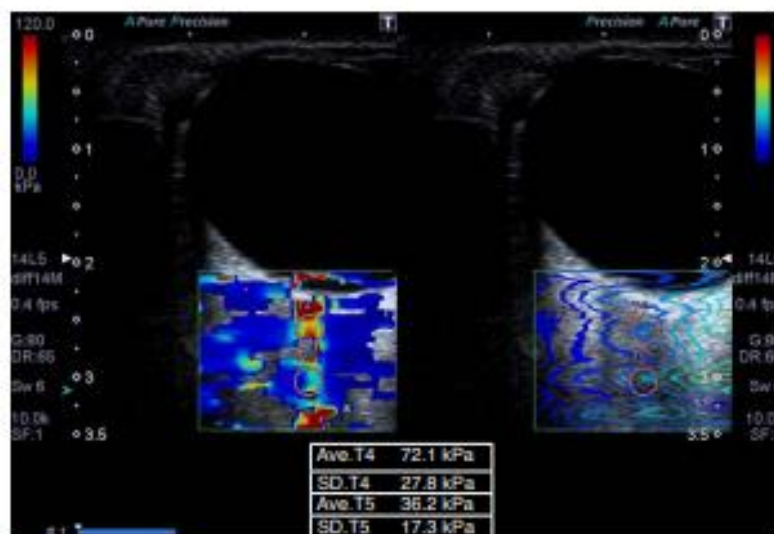
Fig. 1. Optic nerve sheath diameter (ONSD), strain ratio (SR), and shear wave elastography (SWE) of the optic nerve (ON) in a normal control subject.
A–C. ONSD measured on ultrasonography was 4.2 mm. (A), strain elastography shows that the SR of the ON is 0.88 (B), and SWE shows that the SWE of the ON is 12.3 kPa (C).



A

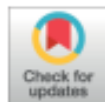


B



C

Fig. 2. Optic nerve sheath diameter (ONSD), strain ratio (SR), and shear wave elastography (SWE) of the optic nerve (ON) in a patient with idiopathic intracranial hypertension (IIH). A–C. Ultrasound image shows an ONSD measurement (7.3 mm) (A), strain elastography shows that the SR of the ON is 0.39 (B), and SWE shows that the SWE of the ON is 36.2 kPa (C). The combined increase in the ONSD, low SR of the ON, and high SWE of the ON helped in the correct diagnosis of IIH.



Comparison of two different lung ultrasound imaging protocols in COVID-19 pneumonia

ULTRA
SONO
GRAPHY

Korgün Ökmen, Durdu Kahraman Yıldız, Emel Soyaslan, İlkay Ceylan, Halil Erkan Sayan, Cihan Sedat Aytünür

Department of Anesthesiology and Reanimation, University of Health Sciences, Bursa Yüksek İhtisas Training and Research Hospital, Bursa, Turkey

ORIGINAL ARTICLE

<https://doi.org/10.14366/usg.21095>
pISSN: 2288-5919 • eISSN: 2288-5943
Ultrasonography 2022;41:212-221

Purpose: The aim of this study was to determine the effectiveness of two different lung ultrasonography (LUS) methods that can be used in the diagnosis of coronavirus disease 2019 (COVID-19) and to investigate their correlations with computed tomography (CT).

Methods: In this prospective, randomized, and single-blind study, 60 patients with COVID-19 were included. The patients were randomized to either the 12-zone LUS group (n=30) or the 14-zone LUS group (n=30). The correlation between LUS and thoracic CT scores was evaluated. As a secondary outcome measure, the characteristic features of the findings of thoracic CT and LUS were examined.

Results: The study was completed with a total of 59 patients. Moderate and high correlations were found between the total CT and LUS scores in the 12-zone and 14-zone study groups. There were no statistically significant differences in the lesion types detected in patients using LUS and CT ($P>0.05$). The left lung lower lobe CT scores were statistically significantly lower in the 14-zone study group than in the 12-zone group ($P=0.019$). The left lower lobe CT and LUS scores were highly correlated in the 14-zone group ($P<0.001$, $r=0.902$).

Conclusion: The results of our study indicated that the two different LUS examination methods performed in different patients had similar findings in terms of the diagnosis and their correlations with CT results.

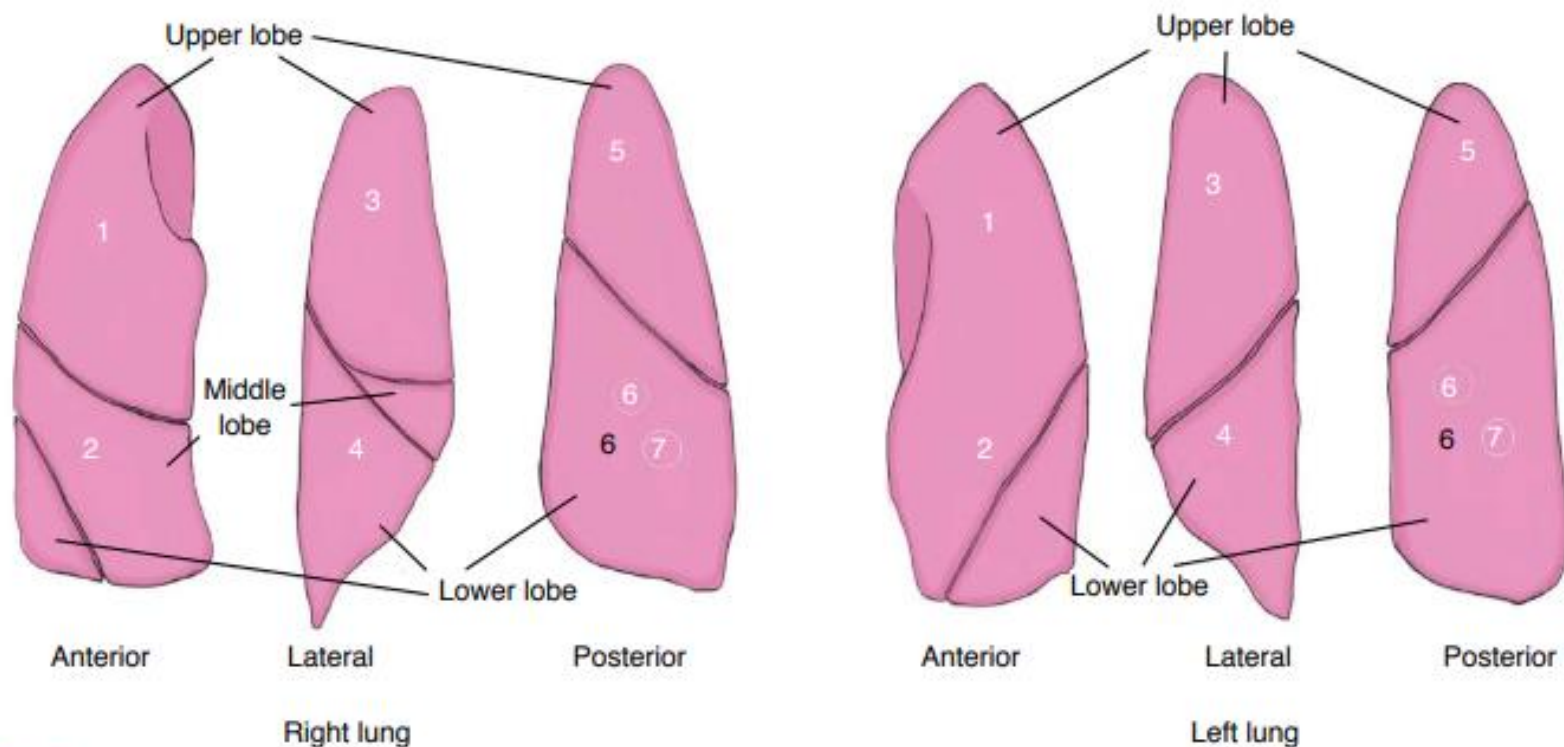
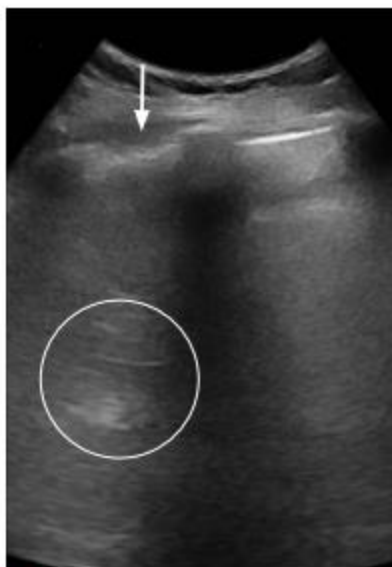


Fig. 2. Lung examination areas. Areas 1–5 are common areas for the 12- and 14-zone evaluations: number 1, upper part of the inter nipple line in the midclavicular line (area 1); number 2, lower part of the inter nipple line in the midclavicular line (area 2); number 3, upper part of the inter nipple line above the midaxillary line (area 3); number 4, lower part of the inter nipple line above the midaxillary line (area 4); number 5, above the line joining the lower ends of the scapula in the paravertebral line (area 5). In the 12-zone group, the posterior-inferior lung region (black number 6) is below the line joining the lower ends of the scapula in the paravertebral line (area 6). In the 14-zone group, the posterior-inferior lung region is divided into multiple areas: the middle area along the paravertebral line at the inferior angle of the shoulder blade (white number 6, area 6) and the basal area along the paravertebral line above the curtain sign (white number 7, area 7).



A

Fig. 3. Lung ultrasonography (LUS) and thoracic computed tomography (CT) images of a 54-year-old woman with coronavirus disease 2019 related pneumonia.

A–C. LUS image (A) of the irregular and thickened pleural line (arrow) of the suppleural lesion (arrow) detected on Thorax CT (B); at the level of the fourth–fifth intercostal space in the middle axillary region (C) is shown.



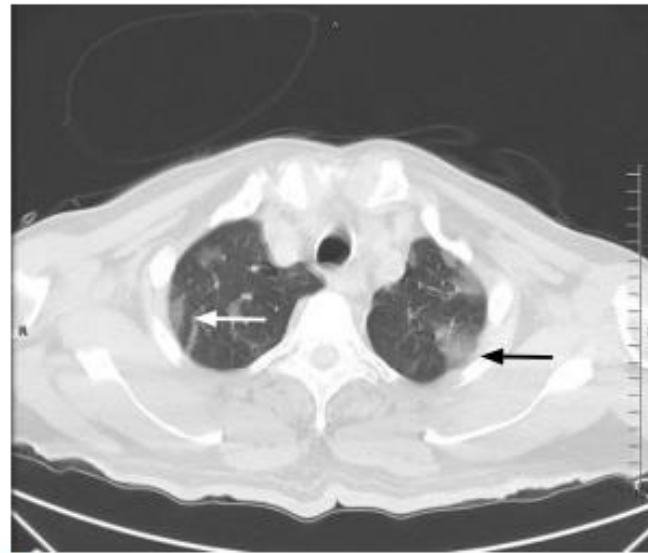
B



C



A



B



C

Fig. 4. Lung ultrasonography (LUS) and thoracic computed tomography (CT) images of a 64-year-old man with coronavirus disease 2019 related pneumonia.

A–C. An irregular and thickened pleural line starting from the subpleural hypoechoic area on LUS (A) is matched to a subpleural consolidation (white arrow) on CT (B). A ground-glass opacity (black arrow) detected in a larger area in the left hemithorax (B) is matched with diffuse B lines of the white lung appearance covering the entire intercostal space on LUS (C).

White paper

Ultrasound Derived Fat Fraction (UDFF)

Michele Baillie, B.Sc, RDMS, RDCS
Siemens Medical Solutions USA Inc.,
Ultrasound Business Area Issaquah, Washington

Aaron Jay Engel, PhD
Siemens Medical Solutions USA Inc.,
Ultrasound Business Area Issaquah, Washington

Arati Gurung, PhD
Siemens Medical Solutions USA Inc.,
Ultrasound Business Area Issaquah, Washington

[siemens-healthineers.com/ultrasound](https://www.siemens-healthineers.com/ultrasound)

Nonalcoholic fatty liver disease is currently the most common cause of chronic liver disease worldwide.³ Fatty liver, or hepatic steatosis, occurs when fat molecules are not metabolized efficiently enough by the body and end up stored in the liver. While a normal liver contains a small amount of fat, the liver is considered “fatty” if the amount of fat within the hepatocytes exceeds 5%.¹

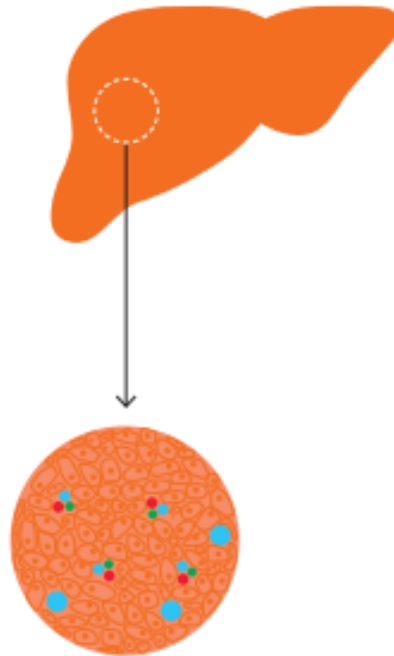
Early detection of hepatic steatosis improves the chances of managing or reversing the condition before irreversible changes can occur.² At present, the existing medical techniques that can diagnose hepatic fat content vary in degrees of effectiveness, cost, invasiveness, availability of equipment, and/or patient suitability. There is a need to develop less invasive and objective quantitative biomarkers for the diagnosis of hepatic steatosis that is cost-effective and widely available.

Ultrasound Derived Fat Fraction (UDFF) is an innovative advanced application available for use on the ACUSON Sequoia ultrasound system that can quantify the amount of fat contained within a patient’s liver. UDFF can quantify fat content in just seconds* during a routine abdominal ultrasound. UDFF delivers a similar clinical utility to MRI Proton Density Fat Fraction (MRI-PDFF) to aid clinicians in determining hepatic steatosis. MRI-PDFF and UDFF methods classify hepatic steatosis as an index value greater than 5%. With the use of this simple tool, physicians now have a new, noninvasive way to help manage adult patients** with hepatic steatosis.

* Based on 5 UDFF acquisitions when used as a stand-alone feature.

** When used as part of an overall assessment of hepatic steatosis.

Normal/healthy liver



Fatty liver

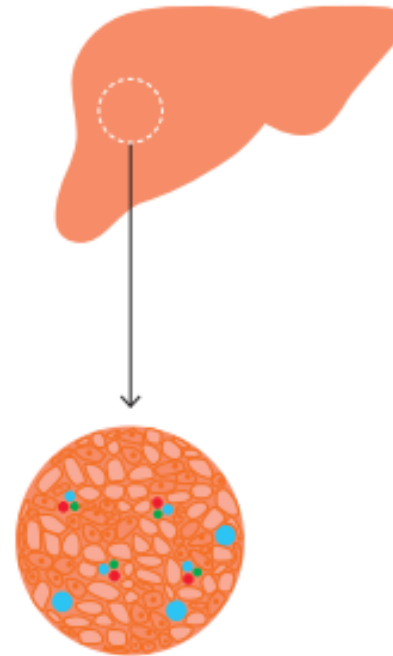


Figure 2: Normal healthy liver tissue compared to fatty liver at a cellular level. Normal liver tissue consists of healthy hepatocytes surrounded by blood vessels and portal triads. In a fatty liver, these hepatocytes become filled with excess fat globules. These globules are stored in the hepatocytes when the body cannot keep up to the metabolic pace that the amount of fat present demands. Histologically, liver fat is graded from 0 to 3 based on hepatocyte fat content. Grade 0 (normal) = <5%, grade 1 (mild) = 5%–33%, grade 2 (moderate) = 34%–66%, and grade 3 (severe) = ≥67%.⁶ The liver is considered fatty when more than 5% of hepatocytes contain fat.








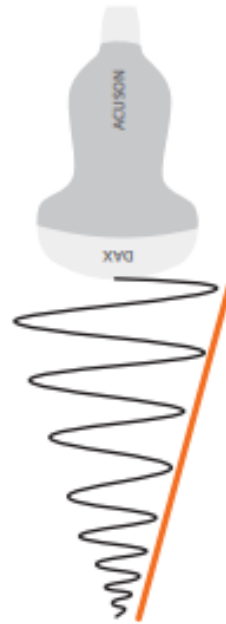
NAFL		NASH				
Normal liver	Steatosis (simple)	Inflammation	Early fibrosis	Significant fibrosis	Cirrhosis	Cirrhosis with HCC
Less than 5% fat ¹	Accumulation of fat in the liver. Steatosis is defined as intrahepatic fat of at least 5% of liver weight ³	Excess fat acts as a toxin and damages healthy liver cells. This results in steatohepatitis (NASH) ^{4,5}	Scar tissue begins to form in the liver as it attempts to repair and replace damaged cells ^{7,9}	Repeated and/or continuous liver damage/repair results in widespread and permanent non-functioning scar tissue ^{7,9}	Extensive scar tissue and regenerated nodules replace most all healthy tissue and inhibits liver function ⁹	Patients with NASH have a 2%–20% 5-year cumulative incidence of hepatocellular carcinoma (HCC) ¹⁰
						

Figure 4: Categories of nonalcoholic fatty liver disease progression from normal liver through to cirrhosis with the potential complication of liver cancer.¹⁰ While not all individuals will progress to a cirrhotic or cancerous state, early knowledge of the presence of disease can allow intervention or treatment that can work toward lowering that risk.

a. No attenuation



b. Moderate attenuation



c. High attenuation



Figure 5: Tissue attenuation can be determined by estimating the frequency content of the sound at different depths then comparing them to values taken from a known reference. This method allows us to isolate the attenuation of the tissue and estimate its attenuation coefficient. In figure 5, the slope of the orange line is related to the attenuation within tissue; the greater slopes indicate greater attenuation coefficient values. No attenuation or almost no attenuation would be seen when imaging in water (a) whereas moderate to high attenuation (b, c) would be seen in soft tissues (liver, kidney, fat etc.).

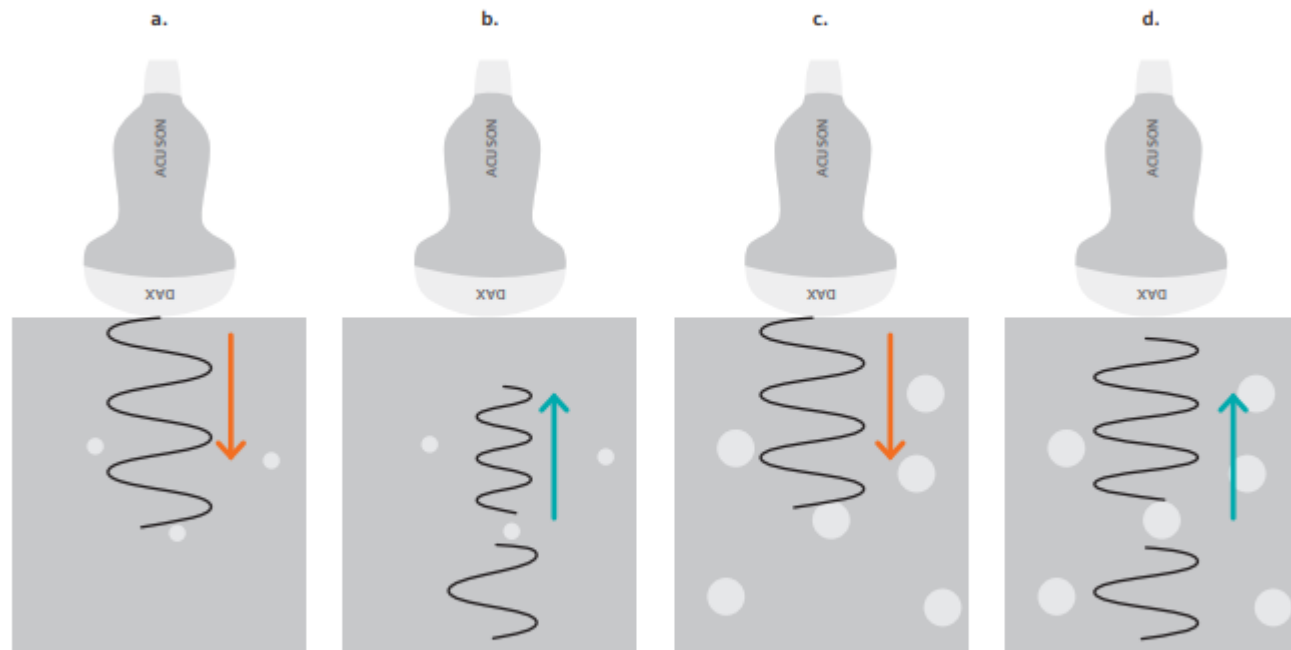


Figure 6: Cell size has a direct influence on the amount of backscatter that occurs. The larger the cell, the greater the degree of sound reflections and scatter that occurs. Figure (a) depicts a small fat particle interacting with the propagating sound wave (orange arrow). When the sound wave interacts with the small fat cell only a small amount of reflection and/or scattering occurs (b, green arrow). Figures (c) and (d) depict the same sound wave interaction but with a larger fat cell. The larger cell produces a greater amount of reflection and/or scattering due to the larger surface area with which the sound wave interacts.

